Design and optimization of lattice structures for aerospace applications

Enrico Stragiotti

François-Xavier Irisarri[1], Cédric Julien[1] and Joseph Morlier[2]

1: ONERA - The French Aerospace Lab
DMAS - Département matériaux et structures
92320 Châtillon, France
{francois-xavier.irisarri, cedric.julien}@onera.fr

2: ICA - Institut Clément Ader
ISAE - SUPAERO
31400 Toulouse, France
joseph.morlier@isae-supaero.fr
January 7, 2024

PhD manuscript

ONERA – ISAE Supaero

Colophon

This document was typeset with the help of KOMA‑Script and L^AT_EX using the kaobook class.

ONERA – ISAE Supaero

CONTENTS

List of Figures

List of Tables

LIST OF ABBREVIATIONS

FEM   Finite Element Method
KS   Kreisselmeier-Steinhauser
LP   Linear Programming
MMA   Method of Moving Asymptotes
MPVCs Mathematical Programs with Vanishing Constraints
NAND   Nested Analysis and Design
SAND   Simultaneous Analysis and Design
SIMP   Solid Isotropic Material with Penalization Method
TTO   Truss Topology Optimization

EVALUATING DISCRETIZATION APPROACHES FOR ULTRALIGHT STRUCTURE OPTIMIZATION

1

check buchi fatti dallo spostamento add equations that are in precedent chapter The process of topology optimization for a structure involves the selection and sizing of optimal elements within a predetermined set. As discussed in the previous chapter, in our context this set could be composed of either continuum elements (shell or volumetric) or truss-like elements. Based on the discretization choice we distinguish between density method topology optimization and Truss Topology Optimization (TTO). This chapter aims to assess the suitability and the inherent advantages and disadvantages of both methods when optimizing ultralight structures i.e. structures that exhibit a low volume fraction, typically below 5%.

For this purpose, we initially formulate a volume minimization problem with maximum stress constraints for both discretizations in Section 1.1. Later, a two-dimensional test case, featuring identical dimensions, loads, and material properties is optimized using the topology optimization and the TTO algorithms. The outcomes of the comparison of both optimization approaches are presented and discussed in Section 1.2.

1.1 THE FORMULATION OF A SHARED PROBLEM: VOLUME MINIMIZATION WITH STRESS CONSTRAINTS

Compared to the compliance minimization formulation, commonly used in classical topology optimization, our focus on the aerospace sector aligns more closely with the volume minimization problem. Prioritizing volume minimization, directly linked to the more crucial mass minimization objective, is driven by economic, environmental, and performance considerations within the aerospace industry. This strategic approach supports industry goals of sustainability, efficiency, and technological advancement. Therefore, we have chosen to adopt the volume minimization optimization formulation for our study, and we will now implement it on both continuum and truss-like meshes.

1.1.1 CONTINUOUS DISCRETIZATION NAND MINIMUM VOLUME FORMULATION

This section introduces the Nested Analysis and Design (NAND) volume minimization formulation for topology optimization on continuum meshes. We will begin by explaining important notations and concepts that are essential for developing the volume minimization formulation.

Objective and constraint functions   The goal of the optimization is to minimize the volume fraction occupied by a structure under a specified load case. In this thesis, as we deal with two- and three-dimensional structures, we should differentiate between area and volume, but for the sake of generality, we talk about volume. The volume fraction of the structure, denoted as V_f, is expressed as the ratio between the structural volume $V = \sum_{i \in \Omega} \bar{\bar{\rho}}_i v_i$ and the total volume (V_0) of the domain Ω:

$$V_\text{f} = \frac{1}{V_0} \sum_{i \in \Omega} \bar{\bar{\rho}}_i v_i. \tag{1.1}$$

We assume that the elementary volume v_i occupied by the i-th element is equal for all the elements, and thus Equation 1.1 is simplified as follows:

$$V_\text{f} = \frac{1}{N_e} \sum_{i \in \Omega} \bar{\bar{\rho}}_i. \tag{1.2}$$

The normalized local stress constraint g_st is formulated as:

$$g_\text{st} := \frac{\sigma_{\text{VM},i}}{\sigma_\text{L}} - 1 \leq 0, \quad \forall i \in \Omega_{mat}(\boldsymbol{\rho}) \tag{1.3}$$

where $\Omega_{mat}(\boldsymbol{\rho}) \subseteq \Omega$ represents the design-dependent set of elements with a non-zero density, $\sigma_{\text{VM},i}$ is the equivalent Von Mises stress for the i-th element, and σ_L is the maximum allowable of the material.

2. Achtziger et al. (2008), 'Mathematical programs with vanishing constraints'

3. Cheng et al. (1992), 'Study on Topology Optimization with Stress Constraints'

The first difficulty that arises is that the stress constraints are defined only for the elements where $\bar{\bar{\rho}}_i > 0$, while $\bar{\bar{\rho}}_i \in [0, 1]$. Thus, the set of constraints changes during the optimization. This class of problems is called Mathematical Programs with Vanishing Constraints (MPVCs) [2] and is known for being difficult to solve with a gradient descent optimization algorithm. The original set of constraints g_st is then reformulated into an equivalent design-independent set of constraints $\bar{g}_\text{st}$ as follows [3]:

$$\bar{g}_\text{st} := \bar{\bar{\rho}}_i \left(\frac{\sigma_{\text{VM},i}}{\sigma_\text{L}} - 1 \right) \leq 0, \quad \forall i \in \Omega. \tag{1.4}$$

Von Mises stress evaluation   The evaluation of the equivalent stress of an element follows the formulation proposed by Von Mises. Let us take a four-node quadrilateral linear element with a single integration (or Gauss) point in the center and four $2a$ equal-length sides (see Fig. 1.1). If bilinear shape functions are used to interpolate the displacement field, we can evaluate the deformations at the

integration point as:

$$\begin{pmatrix} \varepsilon_x \\ \varepsilon_y \\ \gamma_{xy} \end{pmatrix} = B_s q_s, \text{ with } B_s = \frac{1}{4a} \begin{pmatrix} -1 & 1 & 1 & -1 & 0 & 0 & 0 & 0 \\ 0 & 0 & 0 & 0 & -1 & -1 & 1 & 1 \\ -1 & -1 & 1 & 1 & -1 & 1 & 1 & -1 \end{pmatrix},$$

(1.5)

where $q_s = (u_1, u_2, u_3, u_4, v_1, v_2, v_3, v_4)^T$ represents the vector of the displacement degrees of freedom of the element.

The stress tensor is evaluated using the elasticity Hooke's law in 2D as follows:

$$\begin{pmatrix} \sigma_x \\ \sigma_y \\ \tau_{xy} \end{pmatrix} = C_e \begin{pmatrix} \varepsilon_x \\ \varepsilon_y \\ \gamma_{xy} \end{pmatrix} \quad \text{with} \quad C_e = \frac{E}{1-\nu^2} \begin{pmatrix} 1 & \nu & 0 \\ \nu & 1 & 0 \\ 0 & 0 & G \end{pmatrix}.$$

(1.6)

The equivalent Von Mises stress of the element can then be written as:

$$\langle \sigma_{\text{VM}} \rangle = \sqrt{\sigma_x^2 + \sigma_y^2 - \sigma_x \sigma_y + 3\tau_{xy}}$$

(1.7)

$$= \sqrt{\begin{pmatrix} \sigma_x & \sigma_y & \tau_{xy} \end{pmatrix} \begin{pmatrix} 1 & -1/2 & 0 \\ -1/2 & 1 & 0 \\ 0 & 0 & 3 \end{pmatrix} \begin{pmatrix} \sigma_x \\ \sigma_y \\ \tau_{xy} \end{pmatrix}}$$

(1.8)

$$= \sqrt{q_s^T B_s^T C_e^T D_{\text{VM}} C_e B_s q_s}, \text{ with } D_{\text{VM}} = \begin{pmatrix} 1 & -1/2 & 0 \\ -1/2 & 1 & 0 \\ 0 & 0 & 3 \end{pmatrix}$$

(1.9)

$$\langle \sigma_{\text{VM}} \rangle = \sqrt{q_s^T S q_s}, \quad \text{with } S = B_s^T C_e^T D_{\text{VM}} C_e B_s.$$

(1.10)

in which we used the notation introduced by Verbart [4] $\langle \dots \rangle$ to represent macroscopic (or homogenized) variables.

Figure 1.1: A four-node quadrilateral element. GP is the Gaussian integration point for which the equivalent stress is evaluated.

4. Verbart et al. (2017), 'A unified aggregation and relaxation approach for stress-constrained topology optimization'

MICROSCOPIC AND MACROSCOPIC STRESS In stress-constrained topology optimization, the element stress is usually evaluated using the microscopic stress formulation, assuming that there is no direct correlation between stress and density [5]. Indeed, the use of the macroscopic stress in volume minimization optimization problems creates an all-void design [6]. The properties that the microscopic stress should present are:

5. Duysinx et al. (1998), 'Topology optimization of continuum structures with local stress constraints'
6. Le et al. (2010), 'Stress-based topology optimization for continua'

(i) The stress criterion should be mathematically as simple as possible, as the relationship between Young's modulus and density. This permits a simple numerical implementation.

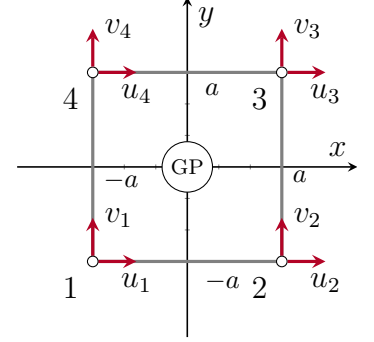(ii) To mimic the real physical behavior, the microscopic stress should be inversely proportional to density.

4. Verbart et al. (2017), 'A unified aggregation and relaxation approach for stress-constrained topology optimization'

(iii) The microscopic stress should converge to a non-zero value at zero density. This requisite is deduced from investigations into the asymptotic stress behavior in thin layers [4].

The relation between stress and displacement is written as:

$$\langle \sigma_{\text{VM}} \rangle = C_e(\langle E \rangle)\langle \varepsilon \rangle, \tag{1.11}$$

where the variables between angular brackets $\langle \dots \rangle$ represent macroscopic variables.

Combining (i) and (ii) with Equations **??**, and 1.11, the microscopic stress can be written as:

$$\sigma_{\text{VM}} = \frac{\langle \sigma_{\text{VM}} \rangle}{\rho_e^q} = \rho_e^{p-q} C_e(E_0)\langle \varepsilon \rangle, \tag{1.12}$$

where the exponent q is a number greater than 1.

4. Verbart et al. (2017), 'A unified aggregation and relaxation approach for stress-constrained topology optimization'
6. Le et al. (2010), 'Stress-based topology optimization for continua'
7. Holmberg et al. (2013), 'Stress constrained topology optimization'
8. Silva et al. (2019), 'Stress-constrained topology optimization considering uniform manufacturing uncertainties'

One possible choice that satisfy all the requirements is $q = p$ [4, 6–8]. Thus, the microscopic stress is defined as:

$$\sigma_{\text{VM}} = C_e(E_0)\langle \varepsilon \rangle. \tag{1.13}$$

The significance of microscopic stress becomes evident when considering an element with intermediate density, that is physically realized by a porous microstructure. The microscopic stress presented in Equation 1.13 measures the stress in the material of the microstructure. It is grounded in the assumption that the macroscopic deformations of the homogenized element generate within the microstructure of the element a stress state that remains unaffected by the density of the element itself.

CONSTRAINTS AGGREGATION AND RELAXATION   When optimizing a structure with stress constraints using a NAND formulation, two primary challenges commonly arise:

9. Rozvany (2001), 'On design-dependent constraints and singular topologies'
10. Stolpe (2003), 'On Models and Methods for Global Optimization of Structural Topology'

11. Sved et al. (1968), 'Structural optimization under multiple loading'

(i) Is it known in the literature [9, 10] that stress-based topology optimization suffers from the *singular minima* (or *singularity*) problem: firstly observed on truss structure optimization [11], these *minima* are almost inaccessible to a standard gradient-based optimizer, often preventing it to reach the global optimum of the optimization [9]. This is because achieving the optimal solution to a problem using continuous design variables may necessitate passing through a state where the optimization constraints are violated, i.e. the *minimum* is on a lower dimension compared to the design space. This problem is often solved using a technique called *constraints relaxation* [12].

12. Cheng et al. (1997), 'ε-relaxed approach in structural topology optimization'

(ii) The stress is a local measure, and thus a large set of constraints is generated when a reasonably fine mesh is used (one element,

one constraint). This problem is often solved using a technique called *constraints aggregation* or *global constraints* [13].

Following the work developed by Verbart *et al.* [4], the lower bound Kreisselmeier-Steinhauser (KS) function [14] is used to approximate the local relaxed stress constraint maximum. The authors showed that employing lower-bound KS aggregation functions to approximate the maximum operator in stress-constrained topology optimization ensures the relaxation and the aggregation of the constraints simultaneously. The KS aggregated stress constraint function is defined as follows:

$$G_{KS}^{L} = \frac{1}{P} \ln \left(\frac{1}{N_e} \sum e^{P \tilde{g}_i} \right). \tag{1.14}$$

Its main advantage over other different formulations is that it uses a single hyperparameter P to control the aggregation and the relaxation of the constraints simultaneously.

Minimum volume formulation   The NAND minimum volume formulation for continuous discretization is written combining Equations 1.2, and 1.14 as:

$$\min_{\rho} \quad V = \frac{1}{N_e} \sum_{i \in \Omega} \bar{\bar{\rho}}_i,$$

$$\text{s.t.} \quad G_{KS}^{L} = \frac{1}{P} \ln \left(\frac{1}{N_e} \sum_{i \in \Omega} e^{P \tilde{g}_i} \right) \leq 0 \tag{$\mathbb{T}_1$}$$

$$\boldsymbol{Ku} = \boldsymbol{F}$$

$$0 \leq \rho_i \leq 1,$$

The optimization is carried out using a gradient descent optimization algorithm for which the sensitivities are given in analytical form. Using analytic gradients is in general more efficient than finite differences as it avoids the need for multiple function evaluations, making the optimization process faster and more precise.

Sensitivity analysis of the objective function   Deriving Equation 1.2 with respect to $\bar{\bar{\rho}}$ we obtain:

$$\frac{\partial V}{\partial \bar{\bar{\rho}}_i} = \frac{1}{N_e}. \tag{1.15}$$

The sensitivity of the objective function can then be evaluated using Equations 1.15, **??**, **??**, and **??** as follows:

$$\frac{dV}{d\rho_i} = \sum_{j \in \mathbb{N}_{i,R}} \frac{\partial V}{\partial \bar{\bar{\rho}}_j} \frac{\partial \bar{\bar{\rho}}_j}{\partial \tilde{\rho}_j} \frac{\partial \tilde{\rho}_j}{\partial \rho_i}. \tag{1.16}$$

13. Silva et al. (2021), 'Local versus global stress constraint strategies in topology optimization'

4. Verbart et al. (2017), 'A unified aggregation and relaxation approach for stress-constrained topology optimization'

14. Kreisselmeier et al. (1979), 'Systematic Control Design by Optimizing a Vector Performance Index'

SENSITIVITY ANALYSIS OF THE CONSTRAINT FUNCTION   The sensitivity of the aggregated constraint function G_{KS}^{L} with respect to the design variable ρ is evaluated using:

$$\frac{dG_{\text{KS}}^{\text{L}}}{d\rho_i} = \sum_{j \in \mathbb{N}_{i,R}} \frac{\partial G_{\text{KS}}^{\text{L}}}{\partial \overline{\overline{\rho}}_j} \frac{\partial \overline{\overline{\rho}}_j}{\partial \widetilde{\rho}_j} \frac{\partial \widetilde{\rho}_j}{\partial \rho_i}. \tag{1.17}$$

As the constraint function $G_{\text{KS}}^{\text{L}} = G(\overline{\overline{\rho}}, \boldsymbol{u}(\overline{\overline{\rho}}))$ is explicitly and implicitly (via the relationship with $\boldsymbol{u}$) depending on $\overline{\overline{\rho}}$, the first-order derivative is evaluated using the total derivative formula:

$$\frac{dG}{d\overline{\overline{\rho}}_j} = \frac{\partial G}{\partial \overline{\overline{\rho}}_j} + \frac{\partial G}{\partial \boldsymbol{u}} \frac{\partial \boldsymbol{u}}{\partial \overline{\overline{\rho}}_j}. \tag{1.18}$$

As function G_{KS}^{L} depends on $\boldsymbol{u}$ via the stresses σ_i, it is possible to write:

$$\frac{\partial G}{\partial \boldsymbol{u}} = \sum_{i \in \Omega} \left(\frac{\partial G}{\partial \sigma_i} \frac{\partial \sigma_i}{\partial \boldsymbol{u}} \right). \tag{1.19}$$

Combining Eq. 1.18 with Eq. 1.19, we obtain:

$$\frac{dG}{d\overline{\overline{\rho}}_j} = \underbrace{\frac{\partial G}{\partial \overline{\overline{\rho}}_j}}_{A} + \sum_{i \in \Omega} \left(\underbrace{\frac{\partial G}{\partial \sigma_i}}_{B} \underbrace{\frac{\partial \sigma_i}{\partial \boldsymbol{u}}}_{C} \right) \underbrace{\frac{\partial \boldsymbol{u}}{\partial \overline{\overline{\rho}}_j}}_{D}. \tag{1.20}$$

We compute the four factors separately:

A –   The first term represents the explicit relationship of G to the physical densities and its calculation is straightforward:

$$\frac{\partial G}{\partial \overline{\overline{\rho}}_j} = \frac{1}{P} \frac{\left(\frac{\sigma_{\text{VM},j}}{\sigma_{\text{L}}} - 1 \right) \frac{1}{N_e} P e^{P \overline{g}_j}}{\frac{1}{N_e} \sum_k e^{P \overline{g}_k}} = \left(\frac{\sigma_{\text{VM},j}}{\sigma_{\text{L}}} - 1 \right) \frac{e^{P \overline{g}_j}}{\sum_k e^{P \overline{g}_k}}. \tag{1.21}$$

B –   The second term can be calculated using the chain rule:

$$\frac{\partial G}{\partial \sigma_i} = \frac{\partial G}{\partial \overline{g}_i} \frac{\partial \overline{g}_i}{\partial \sigma_i} = \frac{1}{P} \frac{\frac{1}{N_e} P e^{P \overline{g}_i}}{\frac{1}{N_e} \sum_k e^{P \overline{g}_k}} \frac{\overline{\overline{\rho}}_i}{\sigma_{\text{L}}} = \frac{\overline{\overline{\rho}}_i}{\sigma_{\text{L}}} \frac{e^{P \overline{g}_i}}{\sum_k e^{P \overline{g}_k}}. \tag{1.22}$$

C –   We reformulate Equation 1.10 to be written in global coordinates instead of local:

$$\sigma_i^2 = \boldsymbol{q}_s^T \boldsymbol{S} \boldsymbol{q}_s = \boldsymbol{u}^T \boldsymbol{S}_g \boldsymbol{u}, \tag{1.23}$$

where $\boldsymbol{S}_g$ represents the matrix $\boldsymbol{S}$ of Equation 1.10 written on global coordinates [1]. We can now differentiate Equation 1.23 with respect of the displacement field in global coordinates $\boldsymbol{u}$ to

1: The matrix $\boldsymbol{S}_g$ can be calculated using the very same assembling approach used for the stiffness matrix $\boldsymbol{K}$ starting from the elemental stiffness matrix $\boldsymbol{K}_e$. As the global stiffness matrix $\boldsymbol{K}$, $\boldsymbol{S}_g$ is symmetric and sparse.

obtain:

$$\frac{\partial \sigma_i}{\partial \boldsymbol{u}} = \frac{S_g \boldsymbol{u}}{\sigma_i}. \tag{1.24}$$

Equations 1.22, and 1.24 are now combined to obtain the result of the product of the **B** and **C** terms. As a result, the derivatives of G with respect to $\boldsymbol{u}$, are written as:

$$\frac{\partial G}{\partial \boldsymbol{u}} = \frac{\frac{\overline{\overline{\rho}}_j}{\sigma_{\mathrm{L}} \sigma_j} e^{P \bar{g}_i}}{\sum_i e^{P \bar{g}_i}} |S_j|_g \boldsymbol{u}. \tag{1.25}$$

D – To calculate the last term, we take the static equilibrium equation $\boldsymbol{K}\boldsymbol{u} = \boldsymbol{f}$ and differentiate it with respect to the physical densities $\overline{\overline{\rho}}_j$, obtaining:

$$\frac{\partial \boldsymbol{K}}{\partial \overline{\overline{\rho}}_j} \boldsymbol{u} + \boldsymbol{K} \frac{\partial \boldsymbol{u}}{\partial \overline{\overline{\rho}}_j} = 0 \iff \frac{\partial \boldsymbol{u}}{\partial \overline{\overline{\rho}}_j} = -\boldsymbol{K}^{-1} \frac{\partial \boldsymbol{K}}{\partial \overline{\overline{\rho}}_j} \boldsymbol{u}, \tag{1.26}$$

where

$$\frac{\partial \boldsymbol{K}}{\partial \overline{\overline{\rho}}_j} = (E_0 - E_{\min}) p \overline{\overline{\rho}}_j^{p-1} \boldsymbol{K}_{e,j}. \tag{1.27}$$

Equation 1.27 represent the well-known first-derivative term of the global stiffness matrix $\boldsymbol{K}$ with respect to the physical densities $\overline{\overline{\rho}}_j$ when using Solid Isotropic Material with Penalization Method (SIMP) material scheme [15]. We obtain the last term:

15. Bendsøe et al. (2004), 'Topology Optimization'

$$\frac{\partial \boldsymbol{u}}{\partial \overline{\overline{\rho}}_j} = -\boldsymbol{K}^{-1} \left((E_0 - E_{\min}) p \overline{\overline{\rho}}_j^{p-1} \boldsymbol{K}_e \right) \boldsymbol{u}. \tag{1.28}$$

Combining Eq. 1.20, Eq. 1.21, Eq. 1.25, and Eq. 1.28, we finally obtain:

$$\frac{\partial G_{\mathrm{KS}}^{\mathrm{L}}}{\partial \overline{\overline{\rho}}_j} = \left(\frac{\sigma_{\mathrm{VM},j}}{\sigma_{\mathrm{L}}} - 1 \right) \frac{e^{P \bar{g}_j}}{\sum_k e^{P \bar{g}_k}} - \boldsymbol{K}^{-1} \frac{\partial G}{\partial \boldsymbol{u}} \left(\frac{\partial \boldsymbol{K}}{\partial \overline{\overline{\rho}}_j} \right) \boldsymbol{u}. \tag{1.29}$$

To avoid the explicit calculation of $\boldsymbol{K}^{-1}$ we use the *adjoint method*[2]. Here is the linear system that, once solved, permits to calculate $\boldsymbol{\psi}$:

2: More information about the adjoint method used to analytically calculate the first-order derivatives can be found on the Martins *et al.* book [16].

$$\boldsymbol{K}\boldsymbol{\psi} = \frac{\partial G}{\partial \boldsymbol{u}} \iff \boldsymbol{\psi} = \boldsymbol{K}^{-1} \frac{\partial G}{\partial \boldsymbol{u}}. \tag{1.30}$$

This formula is called *adjoint equation*. This equation is solved for $\boldsymbol{\psi}$ and the result used to evaluate:

$$\frac{\partial G_{\mathrm{KS}}^{\mathrm{L}}}{\partial \overline{\overline{\rho}}_j} = \left(\frac{\sigma_{\mathrm{VM},j}}{\sigma_{\mathrm{L}}} - 1 \right) \frac{e^{P \bar{g}_j}}{\sum_k e^{P \bar{g}_k}} - \boldsymbol{\psi} \left(\frac{\partial \boldsymbol{K}}{\partial \overline{\overline{\rho}}_j} \right) \boldsymbol{u}. \tag{1.31}$$

Solving linear system 1.30 instead of directly calculating the inverse matrix of $\boldsymbol{K}$ is more efficient from a performance perspective. The cost of solving a system using the Cholesky decomposition is $\mathcal{O}(N^3/3)$, while a matrix inversion is $\mathcal{O}(N^3)$.

where N represents the size of the square matrix describing the linear system. Equation 1.31 represents the first-order derivative equation

used to evaluate the sensitivity of the constraint function $G_{\mathrm{KS}}^{\mathrm{L}}$ with respect to the physical densities $\overline{\overline{\rho}}$. The value of ψ is calculated every iteration solving the linear system 1.30.

1.1.2 Truss discretization SAND minimum volume formulation

We are now shifting our focus from continuous structures to discrete truss systems, describing the Truss Topology Optimization (TTO) (also known in early literature as layout optimization), a structure optimization method that focuses on discrete structures. In his most used formulation, TTO aims at reducing material usage while meeting stress criteria using a Simultaneous Analysis and Design (SAND) approach. The problem is already well-posed for comparison with continuous discretization, and we intend to explore specific key concepts within its established framework. allunga riscrivi il problema di optim e commenta paralelo alla to elenca differenze dal punto di vista della formulazione, elasticita e fem, discretizzazione, linear vs non linear e non convex

1.2 Comparison between continuous topology optimization and TTO

In the upcoming discussion, we will be comparing the optimized structures obtained using discrete and continuous meshes. Our primary objective in this comparison is to choose the the most appropriate method for our study and to gain a better understanding of the application limits inherent in these two structural discretization methods. If, indeed, we identify such limitations, the aim is to discern and define them. Such discussions have already been briefly addressed in the literature [17, 18], but treating the problem without providing numerical results as a basis for making the choice.

Since our interest is in ultralight structures, we are willing to compare the results of both optimization methods when dealing with different volume fractions on a common load case. The volume minimization formulation with stress constraints we use cannot directly control the volume of the optimized structure. For that reason, we decided to adjust the material strength σ_{L} to influence the volume fraction of the optimized structure i.e. employing a more resistant material results in a lower volume fraction and *vice versa*. For this comparative analysis, we have selected three key performance metrics: the volume fraction V_{f}, the structural compliance C, and the maximum material allowable – or strength σ_{L}. Among these, we classify stress limit as the active metric used to influence the optimization, while volume and compliance are the objective of the optimization and a passive metric, respectively. In addition to the aforementioned performance metrics, we will also track the execution time of the algorithms.

17. Bendsøe (1989), 'Optimal shape design as a material distribution problem'
18. Watts et al. (2019), 'Simple, accurate surrogate models of the elastic response of three-dimensional open truss micro-architectures with applications to multiscale topology design'
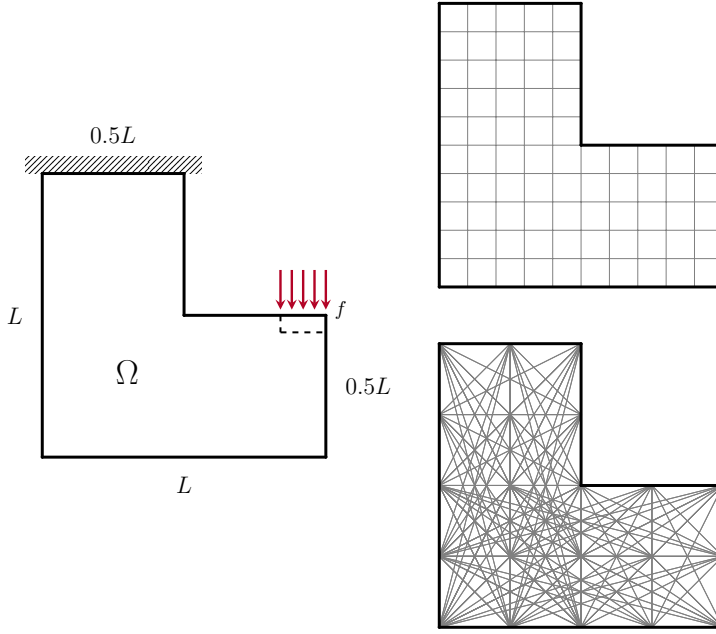
Figure 1.2: On the left, plot of the L-shape beam test case, on the right the graphical representations of the two discretizations used, the continuous (above) composed of 600×600 quadrilateral elements, and the truss-like (below) discretized using 33×33 nodes and a fully connected ground structure. The images represent a coarser discretization for visual clarity.

1.2.1 DEFINITION OF A TEST CASE FOR THE COMPARISON

The L-shape beam is one of the most used load case benchmarks for stress-based topology optimization [5, 6]. This choice is driven by the distinctive geometry of the problem, which generates a stress concentration at the sharp corner in the case of linear elasticity—a phenomenon approaching infinity. Consequently, optimized solutions often feature a large fillet, mitigating the intensity of the stress singularity. The geometric description of the test case is given in Fig. 1.2. The beam with dimensions $L \times L$ presents a fixed support on the nodes in the top part and a load on the right extremity.

To permit the methods' comparison, the design domain Ω is discretized using two distinct meshes: in the continuous case, we employ a mesh consisting of 600×600 quadrilateral elements, totaling $270\,000$ elements. For this mesh, the load is distributed over multiple elements (5% of L) to avoid local stress concentrations. Additionally, the stress constraints are not evaluated on the corresponding elements, and this zone is considered outside of the design domain Ω. Concerning the truss discretization for the TTO algorithm, we employ a mesh with 33×33 nodes and a fully connected ground structure, comprising a total of $305\,728$ candidates. The load is applied only on one single node.

We employ the same isotropic material and structure dimensions for the two optimizations, and the complete data is resumed in Table 1.1. The value of the maximum material allowable σ_L is used to control, although not directly, the volume fraction of the solutions. For simplicity, all numeric values are assumed normalized and dimensionless.

5. Duysinx et al. (1998), 'Topology optimization of continuum structures with local stress constraints'
6. Le et al. (2010), 'Stress-based topology optimization for continua'

Parameter	Value
E	1
ν	0.3
L	100
σ_L	[0.20, 20]

Table 1.1: Material data used for the optimizations. The value of the maximum material allowable σ_L is used as the parameter to generate multiple optimized topologies.

1.2.2 NUMERICAL APPLICATION

The continuous topology optimization and the TTO have both been implemented using Python, employing different optimization algorithms. For continuous topology optimization, the chosen optimization algorithm is the Method of Moving Asymptotes (MMA), developed by Svanberg [19]. The parameter called *movelimit*[3] is set to 0.1 while the other algorithm's parameters are set to their default value. A continuation scheme for the projection parameter β is set to increase by one every 200 iterations and starting from 1, the number of maximum iteration is set to 7500, the stopping criteria is calculated as $\|\Delta x\|_2 / \sqrt{N_e}$ [20] on the absolute difference between two successive iterations of the physical densities $\overline{\overline{\rho}}$, and it is set to 10^{-4}. The aggregation parameter P of the aggregation function G_{KS}^L is set to 32. The optimization is carried out using the NLopt Python optimization package [21], analytically evaluating the sensitivity using Equations 1.15, and 1.20.

The volume minimization TTO problem as formulated in **??** represents a Linear Programming (LP) problem that can be efficiently solved by modern algorithms. In this work, we used the Python package CVXPY 1.2.2 [22] with the ECOS 2.0.7 [23] solver. The joint cost s is set to 0.001 and the stopping criterion is chosen as $\|\Delta x\|_\infty \leq 10^{-8}$. As the formulation is linear, no sensitivity calculation is carried out.

The optimizations presented in this section are performed using a single core on a cluster equipped with an Intel® Xeon® CPU E5-2650 @ 2.20 GHz and using 8 GB of RAM.

CONTINUOUS TOPOLOGY OPTIMIZATION RESULTS We generate multiple optimized structures with different volume fractions V_f by launching the optimization code for continuous mesh with different values of the material allowable σ_L spanning from 0.2 to 20.

The results obtained for $\sigma_L = 10.00, 2.00, 0.40$ and 0.25 are shown in Fig. 1.3. In the upper part of the figure (a-d), we see the topology of the optimized structures with an increasing volume fraction V_f. Interestingly, the topology of the solution remains almost unchanged, varying principally in the thickness of its members. We notice the classic large fillet around the corner that alleviates the local stress concentration. As the volume decreases, the optimized structure tends to a solution that resembles a truss-like structure, with a reducing fillet radius. In those cases, we know that the topology optimization algorithm acts as a method for the layout of truss-like structures [24]. This effect is caused by the combination of different factors, such as the regularization filter, the mesh size, and the low volume fraction [25].

A summary of the numerical results is presented in Table 1.2. Firstly, we can observe how we successfully controlled the volume fraction

19. Svanberg (1987), 'The method of moving asymptotes—a new method for structural optimization'

3: More information on the implementation of the *movelimit* parameter can be found on the paper by Verbart [4].

21. Johnson (2007), 'The NLopt nonlinear-optimization package'

22. Diamond et al. (2016), 'CVXPY: A Python-Embedded Modeling Language for Convex Optimization'
23. Domahidi et al. (2013), 'ECOS: An SOCP solver for embedded systems'

24. Bendsøe et al. (1988), 'Generating optimal topologies in structural design using a homogenization method'
25. Sigmund et al. (2016), 'On the (non-)optimality of Michell structures'
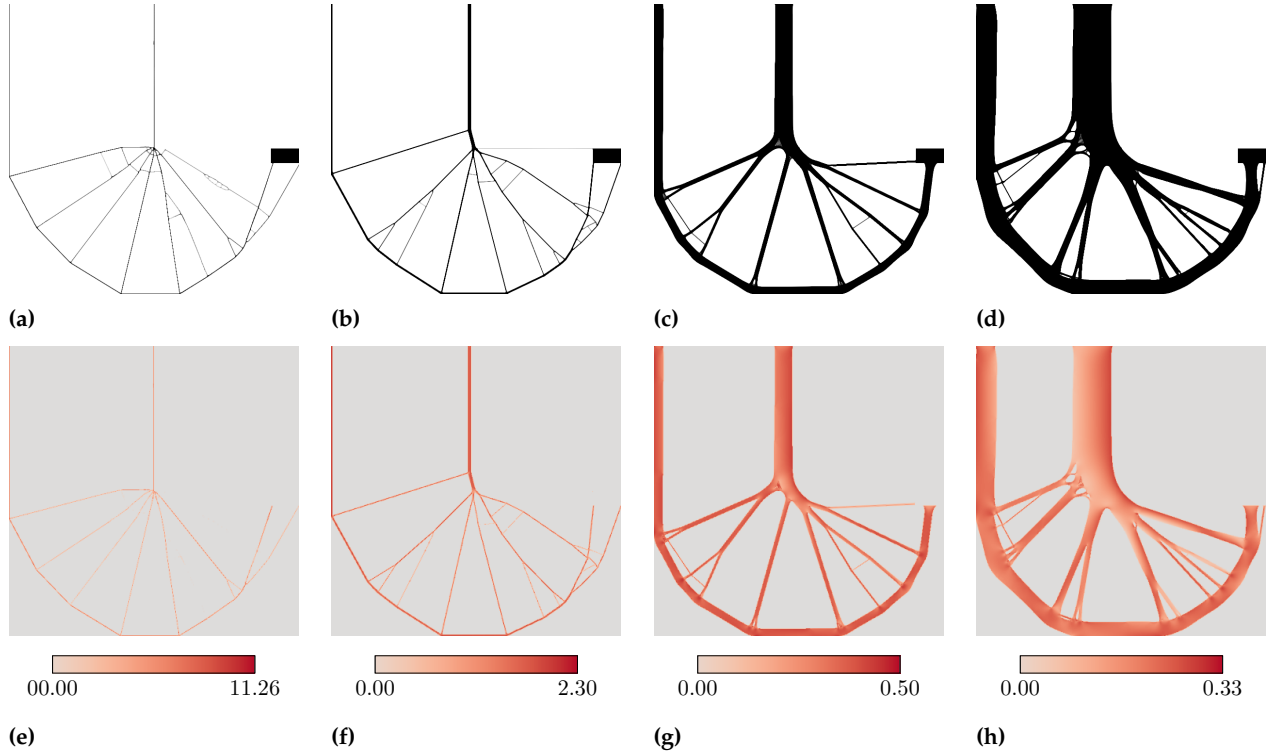
Figure 1.3: (a-d) topology of the optimized structures for different values of the material allowable σ_L = 10.00, 2.00, 0.40, and 0.25, showing a volume fraction of V_f = 1.60%, 4.04%, 18.03% and 34.71%, respectively. (e-h) Von Mises stress distribution for the optimized structures.

V_f by modifying the material resistance σ_L, obtaining results that perfectly follow a monotonically decreasing function. Additionally, as expected, a more voluminous solution also exhibits a lower value of structural compliance. Next, we notice that the optimization processes exhibit long execution times, especially when dealing with extreme cases like low-material resistance and high-volume fractions. This effect is caused by the very fine mesh used to discretize the design domain Ω, the sensitivity calculation using the adjoint method, and the increasing difficulty of satisfying the stress constraints. Furthermore, it is observed that the maximum stress exceeds the material allowable σ_L. This is because we are employing an aggregation function for the stress constraints that estimates the maximum value of the constraint across a group of elements. However, these aggregation methods do not perfectly align with the exact maximum value, which is a recognized limitation.

On top of volume fraction, compliance, and stress, we evaluate an additional metric specific to continuous meshes called the *greyness level* or *measure of non-discreteness* [26] to evaluate the quality of the solutions. It is defined as:

26. Sigmund (2007), 'Morphology-based black and white filters for topology optimization'

$$M_{nd} = \frac{\sum_e 4\overline{\overline{\rho}}_e(1 - \overline{\overline{\rho}}_e)}{n} \times 100\%, \tag{1.32}$$

Table 1.2: Numerical results of the topology optimization method of the L-shape beam load case with varying material allowable σ_L on a 600×600 elements mesh.

σ_L	max σ_L	V_f	C	M_{nd}	It.	Time
20.00	23.51	1.18 %	6992	1.91 %	1142	8 h 11 m
10.00	11.26	1.60 %	3837	2.19 %	1147	7 h 55 m
8.00	8.78	1.74 %	2766	1.95 %	792	5 h 39 m
6.00	7.15	1.89 %	2243	1.81 %	806	5 h 35 m
5.00	5.81	2.17 %	1823	1.81 %	849	5 h 53 m
4.00	4.69	2.67 %	1424	2.02 %	894	6 h 12 m
3.00	3.47	3.00 %	1133	1.64 %	993	6 h 45 m
2.00	2.30	4.04 %	781	1.45 %	1189	8 h 20 m
1.00	1.18	7.28 %	404	1.35 %	1621	11 h 41 m
0.90	1.06	8.09 %	365	1.31 %	1656	11 h 36 m
0.80	0.96	8.82 %	332	1.21 %	1937	15 h 21 m
0.70	0.84	10.05 %	292	1.09 %	1827	13 h 21 m
0.60	0.73	11.80 %	250	1.19 %	1955	14 h 21 m
0.50	0.61	14.18 %	213	1.06 %	2032	15 h 39 m
0.40	0.50	18.03 %	170	1.08 %	2259	17 h 6 m
0.35	0.44	21.12 %	148	1.15 %	2421	19 h 29 m
0.30	0.38	26.21 %	126	1.50 %	3100	24 h 46 m
0.25	0.33	34.71 %	104	1.04 %	3484	27 h 39 m
0.20	0.27	48.08 %	77	1.26 %	7500	91 h 46 m

Michell theorized two criteria for optimal truss structures [27] valid when the maximum allowable stress is equal in tension and compression ($\sigma_t = \sigma_c$) and when the supports of the structure are statically determinate. The first one states that all the members of an optimal structure should present internal stress equal in magnitude to the maximum allowable value of the material – i.e. the structure is *fully stressed*. The second criterion asserts that the strain of all the members of the structure should be equal and there should be no other point having a strain higher than this value.
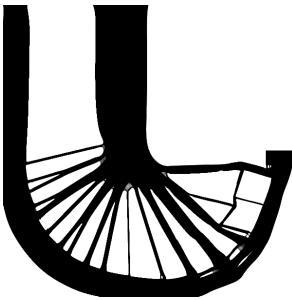

Figure 1.4: The intermediate resulting structure for $\sigma_L = 0.2$ with $V_f = 48.08$ % after 7500 optimization iterations.

where results near zero mean a completely black-and-white design. Observing the M_{nd} values in Table 1.2, we notice that all the optimized structures converged to nearly black-and-white solutions, confirming the correct numerical implementation of the problem.

In the lower part of Fig. 1.3 (e-f), we plot the equivalent Von Mises stress for every element of the solution with physical density $\overline{\overline{\rho}} > 0.5$. Multiple interesting observations can be made. First, we notice that the stress distribution is almost uniform in the structure, and it tends to the value of the material allowable σ_L – i.e. we approach a *fully stressed* structure. Even if the geometric support of the theory is different, it looks like the topology-optimized structures follow the Michell criteria presented in Section **??** for optimal truss structures.

As previously mentioned, our focus lies in exploring the method's limits, particularly at the volume fraction boundaries. When dealing with low-resistance materials – i.e. materials that show a low σ_L, we encounter a scenario where no solution can be attained since no distribution can fulfill the imposed constraints. Throughout our research with this specific test case and mesh size, we did not produce any solutions with a volume fraction exceeding 50%, suggesting we have encountered a limitation of the problem. With this combination of material properties, loading conditions, geometry, and mesh, it appears that there is no feasible solution for $V_f > 50\%$. We notice that the calculation time has significantly increased with the increase of V_f because the algorithm faces greater difficulty in satisfying the stress constraints. Fig. 1.4 shows the topology of the solution with $\sigma_L = 0.2$, $V_f = 48.08$ % and over five days of optimization.

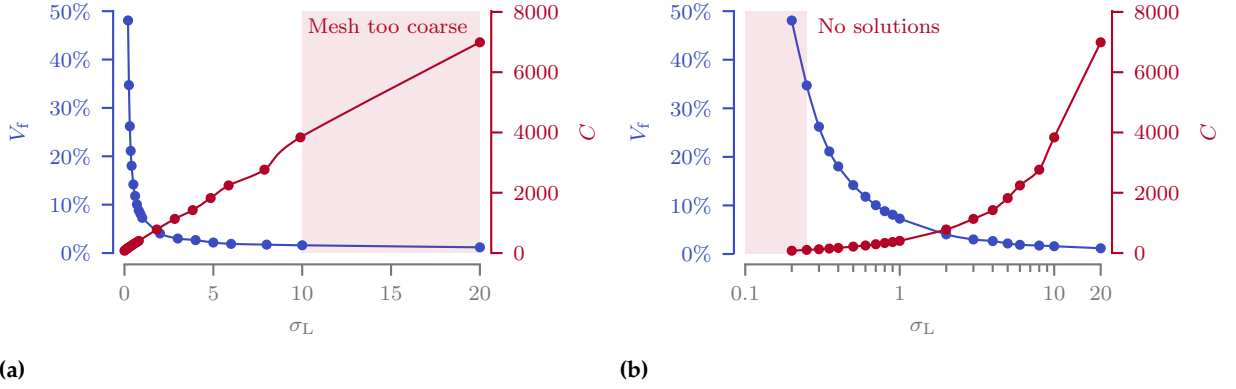Conversely, when dealing with excessively strong material – i.e. mate-

Figure 1.6: Linear (a) and logarithmic (b) plot of the volume fraction V_f and the compliance C with respect to the maximum material allowable σ_L for the continuous mesh structures. Areas in red represent the boundaries of the applied method.

rials that show a high σ_L, the optimal scenario would demand such minimal material usage that certain sections of the structure become thinner than the width of a single element. In this case, the mesh used for discretization is too coarse to accurately represent the solution, and finer meshing becomes essential to capture the details of the optimized design. Fig. 1.5 shows the limit case when $\sigma_L = 10.0$ and $V_f = 1.60\,\%$.

Finally, in Fig. 1.6 we show the plots summarizing our results, with the method's limits highlighted. To effectively show the different orders of magnitude present in the plot, we have used both linear and logarithmic scales simultaneously. We notice that the volume fraction V_f follows a hyperbolic relationship, while compliance C exhibits a linear correlation with respect to the material allowable σ_L.
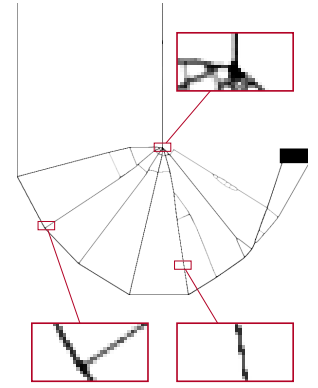
Figure 1.5: The optimized structure for $\sigma_L = 10.0$ with $V_f = 1.60\,\%$. Some of the structure's features present not even a fully-dense element in their thickness.

TTO OPTIMIZATION RESULTS In this section, we present the optimized structures of the TTO formulation with different values of the material allowable σ_L spanning from 0.2 to 20. Due to the inherent linearity of Formulation **??**, the solutions exhibit several intriguing characteristics. Notably, in cases such as the tested L-shaped test case where the structures are not overconstrained and are not subject to asymmetric stress constraints, the formulation aligns with the Michell criteria. Consequently, the topology remains unchanged regardless of the imposed stress limit, and the stress distribution results in a fully stressed structure. Fig. 1.7 provides a visual representation of the optimized topology and the corresponding stress distribution for the different values of the material allowable σ_L. By examining the figure, it is evident that the node positions are constrained by the initial ground structure. The solution resembles half of a spoked wheel, with an irregular distribution of these spokes. One might expect a more evenly distributed arrangement of these spokes. Finally, it is crucial to note that in this simple test case with only a single load case, the linear elasticity is inherently considered in the formulation.

Figure 1.7: Topology (a) and stress distribution (b) plot for the TTO optimized structure of the L-shape beam test case with varying values of the material allowable σ_L on a 33×33 nodes ground structure. The structure topology is invariant with respect to the value of σ_L.
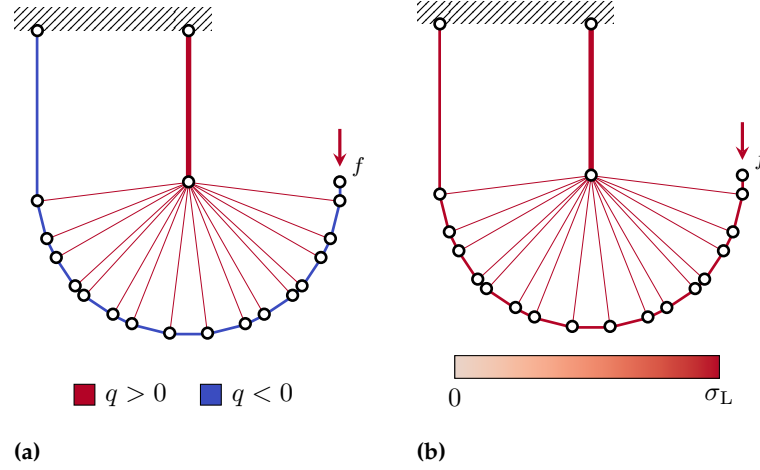
Table 1.3: Numerical results of the TTO method of the L-shape beam test case with varying values of the material allowable σ_L on a 33×33 nodes ground structure.

σ_L	V_f	C	Min λ	Time
50.0	0.12 %	23 282	111.7	1 m 6 s
20.0	0.31 %	9313	70.6	1 m 9 s
10.0	0.62 %	4656	49.9	1 m 18 s
8.0	0.78 %	3725	44.7	1 m 15 s
6.0	1.03 %	2794	38.7	1 m 10 s
5.0	1.24 %	2328	35.3	1 m 24 s
4.0	1.55 %	1863	31.6	1 m 18 s
3.0	2.07 %	1397	27.4	1 m 15 s
2.0	3.10 %	931	22.3	1 m 15 s
1.0	6.21 %	466	15.8	1 m 17 s
0.9	6.90 %	419	15.0	1 m 20 s
0.8	7.76 %	373	14.1	1 m 21 s
0.7	8.87 %	326	13.2	1 m 16 s
0.6	10.35 %	279	12.2	1 m 20 s
0.5	12.42 %	233	11.2	1 m 22 s

There is no need to explicitly account for it by imposing kinematic compatibility constraints, as highlighted in previous studies [15, 28, 29].

15. Bendsøe et al. (2004), 'Topology Optimization'
28. Dorn et al. (1964), 'Automatic design of optimal structures'
29. Hemp (1973), 'Optimum Structures'

The following equation consistently holds for the optimized structures, regardless of the value of σ_L:

$$V^* = \frac{fL}{\sigma_L} \cdot \Gamma, \tag{1.33}$$

30. Lewiński et al. (1994), 'Extended exact solutions for least-weight truss layouts—Part I'

where the volume multiplicative constant Γ depends on the load case and the ground structure used to discretize the design space Ω [30]. For this specific test case with the 33×33 nodes ground structure we found $\Gamma = 4.656$. The execution time of the optimization is approximately 90 s and does not change with respect to the maximum stress σ_L. The full numerical results of the multiple optimizations can be found in Table 1.3.

It's worth noting that we have intentionally opted for a fine mesh here to achieve an element count roughly equivalent to that of the

continuous mesh case (305 728 and 270 000 for the TTO and the continuous topology optimization, respectively). We have utilized a fully connected ground structure with 33×33 nodes, but we obtain satisfactory results with just 13×13 nodes (see Fig. 1.8). In this case we obtain a volume multiplicative constant $\Gamma = 4.705$, signifying a 1.05 % increase compared to the 33×33 case with $\Gamma = 4.656$. However, the element number is reduced by 97.4 % (305 728 versus 7705 candidates). The computational time for this simplified test case is below one second.

With this example we notice that refining the continuous mesh and refining the ground structure are not equivalent operations. In one case, it allows for representing finer details, while in the other, it permits new shapes for the structure. The choice of the ground structure dictates the final form; it is more restrictive than merely allowing finer details. If bars are missing initially, they will not be added later on.

In assessing solution quality, we employ a distinct metric known as the slenderness ratio, denoted as λ, which represents the ratio between the length and the radius of gyration of the bars of the ground structure. In our specific case, we have established a minimum slenderness ratio of 15. For a bar with a circular cross-sectional area, this corresponds to a radius of R_λ for a bar length of 7.5 R_λ. We higlighted in red the optimized structures that does not respect the minimum slenderness ratio in Table 1.3.

Lastly, Fig. 1.9 provides a visual summary of our findings, emphasizing in red the solutions that do not respect the minimum slenderness ratio $\lambda < 15$. To effectively show the different orders of magnitude present in the plot and how already done for the continuous mesh case, we have used both linear and logarithmic scales simultaneously. In this case, the compliance exhibits a perfectly linear relationship with respect to σ_L, while the volume follows a hyperbolic law in accordance with Equation 1.33.

1.2.3 Discussion

Up until now, we have discussed the results of the continuous topology optimization and the TTO algorithms separately. Here, we provide a comparative analysis by presenting a series of graphs showcasing three key performance indicators considered for both formulations: the maximum material allowable stress σ_L, the compliance C, and the volume fraction V_f. It is important to note that the data presented in these graphs excludes the values that fall outside the methods' limits, highlighted for the two different algorithms in the previous subsections.

Fig. 1.10 depicts the compliance C versus maximum material allowable σ_L graph for the L-shaped beam test case. It is evident that the truss

Figure 1.8: Optimized structure obtained using a fully connected ground structure with 13×13 nodes and 7705 candidates.
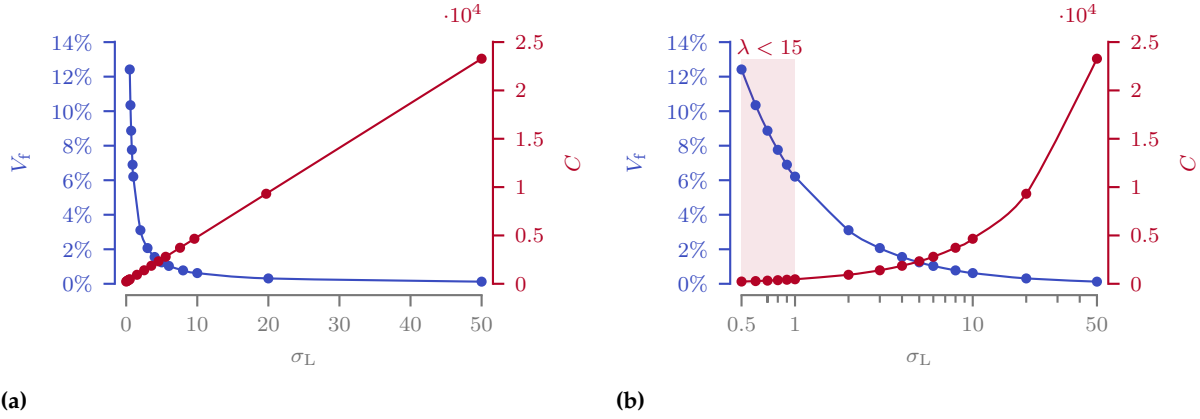
Figure 1.9: Linear (a) and logarithmic (b) plot of the volume fraction V_f and the compliance C with respect to the value of the maximum material allowable σ_L for the TTO optimized structures. Areas in red represent the zones outside the domains of applicability of the truss discretization.
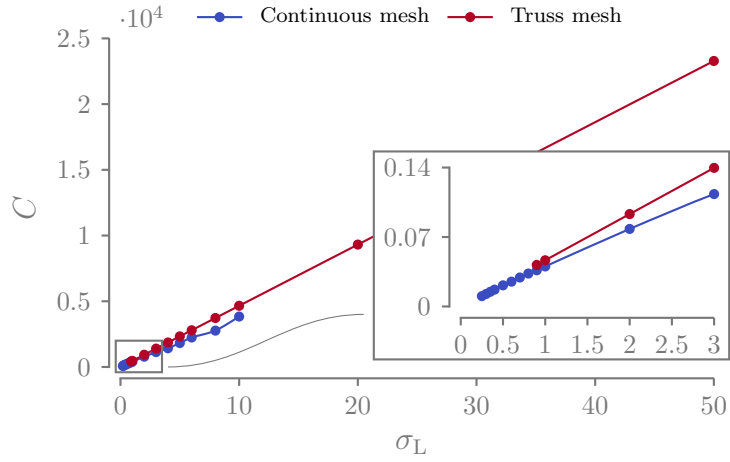

Figure 1.10: Compliance C versus maximum material allowable σ_L plot for the continuous topology optimization and the TTO algorithms.

discretization of TTO consistently exhibits lower compliance values for every considered material allowable and maintains a perfectly linear relationship, in contrast to the continuous discretization approach. We speculate that the difference may be attributed to the more complex formulation (non-linearity, use of the filter and projection), potentially causing the continuous approach to converge to a local minimum. It is worth noting that the differences between the two methods reduce for small σ_L values.

In Fig. 1.11 we plot the different volume fractions obtained for a given material allowable (the axis in the graph are swapped as for us the most important figure of merit is the volume fraction). The continuous topology optimization yields structures that are more massive for a given material resistance. This outcome can be attributed not only to the aforementioned non-linearity in the formulation but also to another intriguing phenomenon. When dealing with high volume fractions (see e.g. Fig. 1.3c and d), we observe that the material that compose the "beams" of the structure is distributed across multiple elements, appearing somewhat "smeared". In contrast, the truss representation concentrates all the structural mass along the line
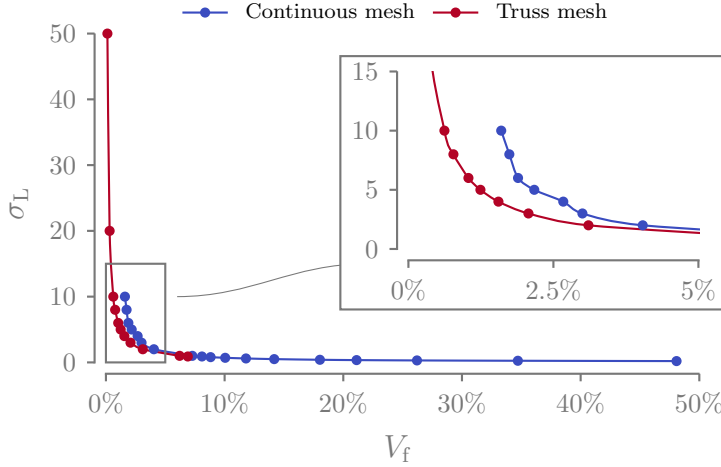
Figure 1.11: Maximum material allowable σ_{L} versus volume fraction V_{f} plot for the continuous topology optimization and the TTO algorithms.
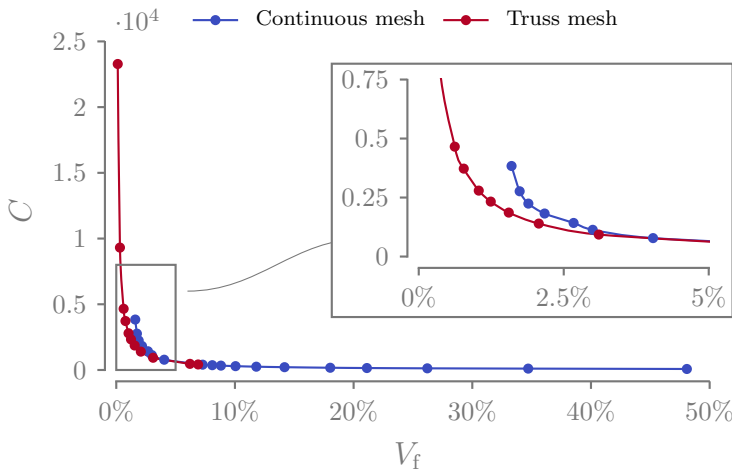

Figure 1.12: Compliance C versus volume fraction V_{f} plot for the continuous topology optimization and the TTO algorithms.

extending from one node to another, putting the material exactly where needed and being, thus, numerically more efficient. This fact happens because the truss representation is an idealization, and it emphasizes the importance of ensuring that the chosen discretization remains within its applicable domain.

We can also observe that the truss representation serves as the lower limit of the topology optimization. We speculate that improving the convergence of the continuous topology optimization could potentially lead to results approaching those provided by the TTO algorithm. Interestingly, both discretizations follow a similar trend for high-volume fractions, despite the significant disparity in their physical description models. The very same trends can be observed watching the volume-complaince graph of Fig. 1.12.

Finally, in Fig. 1.13 we turn our attention to the computational time comparison between the two optimization methods. It is noteworthy that a consistent three-order of magnitude difference is observed between the two methods (days vs. minutes) for every value of V_{f}. Additionally, it's worth recalling that for this specific test case, employing an extremely fine ground structure is not always a necessity,

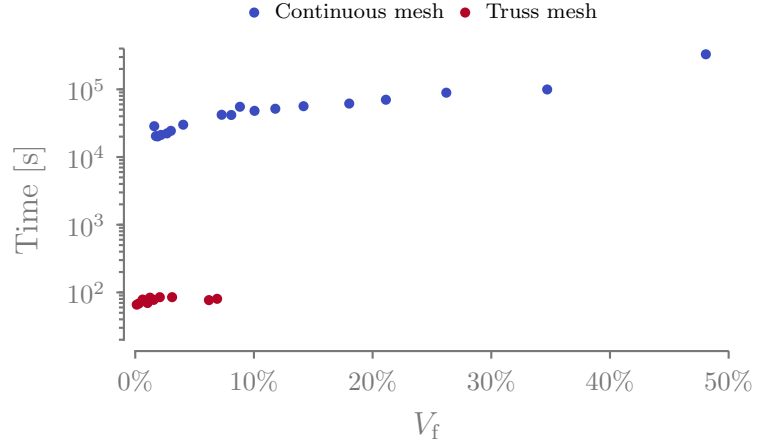**Figure 1.13:** Computational time t versus volume fraction V_f plot for the continuous topology optimization and the TTO algorithms.

as we were able to obtain similar results (slightly more than 1 % volume difference) with coarser ground structures (97 % fewer bars). This fact implies that the calculation time difference between continuous topology optimization and TTO could potentially be even bigger.

The notable difference in computation time for stress-based continuous topology optimization (which is not self-adjoint, in contrast to compliance minimization) points to the potential for exploring SAND approaches for continuous topology optimization. It's worth mentioning that SAND approaches typically lead to a substantial increase in the number of design variables[4], but could beneficial when advanced mechanical constraints are used. In TTO problems, this is less of a concern due to the use of the ground structure approach, which results in numerous cross-sectional area design variables and fewer displacement-related ones. This, however, does not hold when dealing with a continuous mesh. While preliminary studies in this direction have been conducted [31], they lie beyond the scope of this thesis and will not be further investigated.

4: In the SAND approach the displacements u are no more evaluated using the linear Finite Element Method (FEM) equation $Ku = f$, but used as design variables of the optimization.

31. Munro et al. (2017), 'Local stress-constrained and slope-constrained SAND topology optimisation'

To sum up, the advantages of the TTO optimization algorithm become evident when considering the limitations of continuous discretization for optimizing ultralight structures. The first key drawback of continuous topology optimization is its increasing need for more elements to correctly discretize low-volume fraction structures, substantially augmenting computational time. Additionally, continuous topology optimization faces several numerical challenges, such as the need for constraints aggregation and relaxation. The optimization formulation proposed in this chapter addresses these problems but introduces another drawback: stress limit in optimized structures often exceed the specified allowable limit. Strategies exist to address this issue, but they come at the cost of increased computation time. Furthermore, stress constraints in continuous discretization are often defined for equivalent von Mises stress, making it more challenging to distinguish between asymmetric bounds for tension and compression. New failure criteria should then be implemented. Finally, the optimization of

ultralight structures naturally tends to result in truss-like topologies regardless of the chosen optimization formulation. These structures are naturally subject to local buckling as a mode of failure [25], a phenomenon that is difficult to describe when using continuous elements.

While truss discretization offers advantages in terms of computational efficiency, it does come with certain limitations. In the minimum volume formulation, the problem is linear and cost-effective to solve. However, the linearity is lost when additional constraints, such as local buckling, are introduced. Moreover, as the FEM equation $Ku = f$ is never explicitly solved during the optimization, the SAND formulation does not inherently account for the kinematic compatibility of the displacements and the forces of the problem. This limitation restricts its applicability to relatively simple problems, as those presented in this chapter, where kinematic compatibility was inherently satisfied. Issues can arise, however, when dealing with complex scenarios involving multiple loads or constraints that may lead to structures that are statically indeterminate. However, these limitations are well-known in the literature of TTO and should be taken into account during the optimization if we decide to pursue the development of the optimization algorithm using the TTO framework.

1.3 CONCLUSION

Since the first developments of the topology optimization method, it has been recognized that "For moderately low volume fractions the lay-out of truss-like structures is predicted, but for very low volume fractions it is recommended that the traditional lay-out theory be employed..." [17]. However, the performance gap has never been quantified, nor has the domain of applicability been assessed. Additionally, it's important to note that these assumptions were primarily based on compliance formulations and not on volume minimization formulations, which are more pertinent to the aeronautical context.

In this chapter, we assessed the suitability of employing the TTO algorithm for the optimization of ultralight structures by quantifying the disparities between continuous topology optimization and TTO under the volume minimization under strength constraints formulation. We introduced a standardized two-dimensional test case, the L-shaped beam, commonly utilized in stress-based optimization scenarios. Multiple optimization runs were conducted for both discretization methods, employing various materials, and the results were subsequently compared, with a primary focus on volume fraction, compliance, and stress in the optimized structures.

Considering the limitations encountered with the continuous approach, particularly at very low volume fractions, we opted to pursue

25. Sigmund et al. (2016), 'On the (non-)optimality of Michell structures'

17. Bendsøe (1989), 'Optimal shape design as a material distribution problem'

The sensitivity calculation is easier, as the different design variables are not explicitly dependent on each other.

our optimization algorithm development using the Truss Topology Optimization (TTO) framework. The use of a ground structure to discretize the design space is more coherent with the type of structures we are working on, and the use of the SAND approach permits to drastically reduce the computational time and to take into account additional constraints more easily . We also identified certain limitations inherent to truss discretizations, namely the need to take into account the kinematic compatibility of the structure and the local buckling failure mode, which will be addressed in the following chapter.

Bibliography

[1]   Stragiotti, Enrico, Irisarri, François-Xavier, Julien, Cédric, and Morlier, Joseph, 'Towards manufactured lattice structures: a comparison between layout and topology optimization', *AeroBest 2021 International Conference on Multidisciplinary Design Optimization of Aerospace Systems. Book of proceedings*, Lisbon, Portugal: ECCOMAS, July 2021, pp. 229–244.

cited on page 1

[2]   Achtziger, Wolfgang and Kanzow, Christian, 'Mathematical programs with vanishing constraints: optimality conditions and constraint qualifications', *Mathematical Programming* 114.1 (July 2008), pp. 69–99.
DOI: 10.1007/s10107-006-0083-3

cited on page 2

[3]   Cheng, Gengdong and Jiang, Zheng, 'Study on Topology Optimization with Stress Constraints', *Engineering Optimization* 20.2 (Nov. 1992), pp. 129–148.
DOI: 10.1080/03052159208941276

cited on page 2

[4]   Verbart, Alexander, Langelaar, Matthijs, and Keulen, Fred van, 'A unified aggregation and relaxation approach for stress-constrained topology optimization', *Structural and Multidisciplinary Optimization* 55.2 (Feb. 2017), pp. 663–679.
DOI: 10.1007/s00158-016-1524-0

cited on pages 3–5, 10

[5]   Duysinx, P. and Bendsøe, M. P., 'Topology optimization of continuum structures with local stress constraints', *International Journal for Numerical Methods in Engineering* 43.8 (1998), pp. 1453–1478.
DOI: 10.1002/(SICI)1097-0207(19981230)43:8<1453::AID-NME480>3.0.CO;2-2

cited on pages 3, 9

[6]   Le, Chau, Norato, Julian, Bruns, Tyler, Ha, Christopher, and Tortorelli, Daniel, 'Stress-based topology optimization for continua', *Structural and Multidisciplinary Optimization* 41.4 (Apr. 2010), pp. 605–620.
DOI: 10.1007/s00158-009-0440-y

cited on pages 3, 4, 9

[7]   Holmberg, Erik, Torstenfelt, Bo, and Klarbring, Anders, 'Stress constrained topology optimization', *Structural and Multidisciplinary Optimization* 48.1 (2013), pp. 33–47.
DOI: 10.1007/s00158-012-0880-7

cited on page 4

[8]   Silva, Gustavo Assis da, Beck, André Teófilo, and Sigmund, Ole, 'Stress-constrained topology optimization considering uniform manufacturing uncertainties', *Computer Methods in Applied Mechanics and Engineering* 344 (Feb. 2019), pp. 512–537.
DOI: 10.1016/j.cma.2018.10.020

cited on page 4

cited on page 4

[9] Rozvany, G.I.N., 'On design-dependent constraints and singular topologies', *Structural and Multidisciplinary Optimization* 21.2 (Apr. 2001), pp. 164–172.
DOI: 10.1007/s001580050181

cited on page 4

[10] Stolpe, Mathias, 'On Models and Methods for Global Optimization of Structural Topology', Publisher: Matematik, PhD thesis, 2003.

cited on page 4

[11] Sved, G. and Ginos, Z., 'Structural optimization under multiple loading', *International Journal of Mechanical Sciences* 10.10 (Oct. 1968), pp. 803–805.
DOI: 10.1016/0020-7403(68)90021-0

cited on page 4

[12] Cheng, G. D. and Guo, X., 'ε-relaxed approach in structural topology optimization', *Structural optimization* 13.4 (June 1997), pp. 258–266.
DOI: 10.1007/BF01197454

cited on page 5

[13] Silva, Gustavo Assis da, Aage, Niels, Beck, André Teófilo, and Sigmund, Ole, 'Local versus global stress constraint strategies in topology optimization: A comparative study', *International Journal for Numerical Methods in Engineering* 122.21 (2021), pp. 6003–6036.
DOI: 10.1002/nme.6781

cited on page 5

[14] Kreisselmeier, G. and Steinhauser, R., 'Systematic Control Design by Optimizing a Vector Performance Index', *IFAC Proceedings Volumes*, IFAC Symposium on computer Aided Design of Control Systems, Zurich, Switzerland, 29-31 August 12.7 (Sept. 1979), pp. 113–117.
DOI: 10.1016/S1474-6670(17)65584-8

cited on pages 7, 14

[15] Bendsøe, Martin P. and Sigmund, Ole, 'Topology Optimization'. Berlin, Heidelberg: Springer Berlin Heidelberg, 2004.
ISBN: 978-3-642-07698-5 978-3-662-05086-6

cited on page 7

[16] Martins, Joaquim R. R. A. and Ning, Andrew, 'Engineering Design Optimization', 1st ed. Cambridge University Press, Nov. 2021.
ISBN: 978-1-108-98064-7 978-1-108-83341-7

cited on pages 8, 19

[17] Bendsøe, M. P., 'Optimal shape design as a material distribution problem', *Structural optimization* 1.4 (Dec. 1989), pp. 193–202.
DOI: 10.1007/BF01650949

cited on page 8

[18] Watts, Seth, Arrighi, William, Kudo, Jun, Tortorelli, Daniel A., and White, Daniel A., 'Simple, accurate surrogate models of the elastic response of three-dimensional open truss micro-architectures with applications to multiscale topology design', *Structural and Multidisciplinary Optimization* 60.5 (Nov. 2019), pp. 1887–1920.
DOI: 10.1007/s00158-019-02297-5

[19] Svanberg, Krister, 'The method of moving asymptotes—a new method for structural optimization', *International Journal for Numerical Methods in Engineering* 24.2 (1987), pp. 359–373. DOI: https://doi.org/10.1002/nme.1620240207

cited on page 10

[20] Ferrari, Federico and Sigmund, Ole, 'A new generation 99 line Matlab code for compliance topology optimization and its extension to 3D', *Structural and Multidisciplinary Optimization* 62.4 (Oct. 2020), pp. 2211–2228. DOI: 10.1007/s00158-020-02629-w

cited on page 10

[21] Johnson, Steven G., 'The NLopt nonlinear-optimization package', https://github.com/stevengj/nlopt, 2007.

cited on page 10

[22] Diamond, Steven and Boyd, Stephen, 'CVXPY: A Python-Embedded Modeling Language for Convex Optimization', 2016.

cited on page 10

[23] Domahidi, Alexander, Chu, Eric, and Boyd, Stephen, 'ECOS: An SOCP solver for embedded systems', *2013 European Control Conference (ECC)*, Zurich: IEEE, July 2013, pp. 3071–3076, ISBN: 978-3-033-03962-9. DOI: 10.23919/ECC.2013.6669541

cited on page 10

[24] Bendsøe, Martin Philip and Kikuchi, Noboru, 'Generating optimal topologies in structural design using a homogenization method', *Computer Methods in Applied Mechanics and Engineering* 71.2 (Nov. 1988), pp. 197–224. DOI: 10.1016/0045-7825(88)90086-2

cited on page 10

[25] Sigmund, Ole, Aage, Niels, and Andreassen, Erik, 'On the (non-)optimality of Michell structures', *Structural and Multidisciplinary Optimization* 54.2 (Aug. 2016), pp. 361–373. DOI: 10.1007/s00158-016-1420-7

cited on pages 10, 19

[26] Sigmund, Ole, 'Morphology-based black and white filters for topology optimization', *Structural and Multidisciplinary Optimization* 33.4 (Apr. 2007), pp. 401–424. DOI: 10.1007/s00158-006-0087-x

cited on page 11

[27] Michell, A. G. M., 'The limits of economy of material in frame-structures', *The London, Edinburgh, and Dublin Philosophical Magazine and Journal of Science* 8.47 (Nov. 1904), pp. 589–597. DOI: 10.1080/14786440409463229

cited on page 12

[28] Dorn, W. S., Gomory, Ralph E., and Greenberg, H., 'Automatic design of optimal structures', *J. Mécanique* (1964).

cited on page 14

[29] Hemp, W. S., 'Optimum Structures'. Clarendon Press, 1973, Google-Books-ID: cJhpAAAAMAAJ. ISBN: 978-0-19-856110-1

cited on page 14

[30] Lewiński, T., Zhou, M., and Rozvany, G. I. N., 'Extended exact solutions for least-weight truss layouts—Part I: Cantilever with a horizontal axis of symmetry', *International Journal of Mechanical Sciences* 36.5 (1994), pp. 375–398.

cited on page 14

DOI: `10.1016/0020-7403(94)90043-4`

cited on page 18

[31] Munro, Dirk and Groenwold, Albert, 'Local stress-constrained and slope-constrained SAND topology optimisation', *International Journal for Numerical Methods in Engineering* 110.5 (May 2017), pp. 420–439.
DOI: `10.1002/nme.5360`